Biomaterials Science

PAPER

View Article Online
View Journal | View Issue

Cite this: *Biomater. Sci.*, 2019, **7**, 1565

La-Doped mesoporous calcium silicate/chitosan scaffolds for bone tissue engineering†

Xiao-Yuan Peng, ‡[a] Min Hu,‡[b] Fang Liao,[b] Fan Yang,[a] Qin-Fei Ke,[b] Ya-Ping Guo *[b] and Zhen-Hong Zhu *[a]

Received 17th November 2018,
Accepted 13th January 2019

DOI: 10.1039/c8bm01498a

rsc.li/biomaterials-science

Trace rare earth elements such as lanthanum (La) regulated effectively bone tissue performances; however, the underlying mechanism remains unknown. In order to accelerate bone defects especially in patients with osteoporosis or other metabolic diseases, we firstly constructed lanthanum-doped mesoporous calcium silicate/chitosan (La-MCS/CTS) scaffolds by freeze-drying technology. During the freeze-drying procedure, three-dimensional macropores were produced within the La-MCS/CTS scaffolds by using ice crystals as templates, and the La-MCS nanoparticles were distributed on the macropore walls. The hierarchically porous structures and biocompatible components contributed to the adhesion, spreading and proliferation of rat bone marrow-derived mesenchymal stem cells (rBMSCs), and accelerated the in-growth of new bone tissues. Particularly, the La^{3+} ions in the bone scaffolds remarkably induced the osteogenic differentiation of rBMSCs *via* the activation of the TGF signal pathway. A critical-sized calvarial-defect rat model further revealed that the La-MCS/CTS scaffolds significantly promoted new bone regeneration as compared with pure MCS/CTS scaffolds. In conclusion, the La-MCS/CTS scaffold showed the prominent ability in osteogenesis and bone regeneration, which showed its application potential for bone defect therapy.

Introduction

Bone defects derived from traumas, disease-related injuries and surgical resections lead to local dysfunction, and even do great harm to human health.[1,2] Based on bone tissue engineering, various promising biomaterials such as hydroxyapatite (HA), β-tricalcium phosphate (β-TCP), calcium silicate (CS), gelatin (Gel) and chitosan (CTS) have been constructed for repairing damaged bone tissues.[3–5] The above bone materials show good osteoconductivity, biodegradability and biocompatibility, but their limited osteoinductivity holds them back from orthopedic applications. In order to enhance the bone-forming activity of biomaterials, it is an important strategy to controllably regulate their components and microstructures.[6,7] The positive interaction between materials and cells/tissues facilitates osteoblast proliferation and bone tissue regeneration.

Calcium silicate is one of the promising biocompatible ceramics that can provide an appropriate microenvironment for accelerating *in vivo* bone tissue regeneration.[8,9] On one hand, the Ca^{2+} ions in calcium silicate are the main chemical components for newly formed bones; on the other hand, the as-biodegraded Si element not only can trigger osteogenic differentiation of stem cells *via* upregulating MEK and PKC pathways, but also can accelerate new bone deposition.[10–12] Notably, the bioactivity of calcium silicate ceramics should be further improved in order to facilitate the effective treatment of bone defects especially for patients with metabolic disorders.[13] Fortunately, the incorporation of bioactive elements is an alternative strategy to enhance new bone formation capacity.[14] Interestingly, the La element that easily substitutes for the Ca element in HA crystals is found in human bones and can remarkably regulate bone biomineralization and metabolism.[15,16] Lanthanum-based complexes or compounds have been employed as active agents to treat bone density diseases, which stimulate bone formation without accelerating bone resorption.[17] Notably, the biological properties of rare earth elements (REEs) are believed to be hormetic concentration-related effects. Low La concentrations show beneficial and positive effects, while high La concentrations are toxic to healthy cells/tissues.[18] Bai *et al.* have reported that the viability of bone marrow stromal cells (BMSCs) is enhanced by $LaCl_3$ with a low concentration of 10^{-9} M.[15] If the low concentrations

[a]*Department of Orthopedic Surgery, Shanghai Jiao Tong University Affiliated Sixth People's Hospital, Shanghai 200233, P. R. China. E-mail: zzhwz@21cn.com*
[b]*The Education Ministry Key Lab of Resource Chemistry and Shanghai Key Laboratory of Rare Earth Functional Materials, Shanghai Normal University, Shanghai 200234, China. E-mail: ypguo@shnu.edu.cn*

†Electronic supplementary information (ESI) available. See DOI: 10.1039/c8bm01498a

‡These authors contributed equally.

are kept at 10^{-5} M, $LaCl_3$ may induce cell apoptosis.[15] In order to display positive effects and avoid toxic side effects on organisms, *in vivo* La^{3+} ions must be controlled in the safe concentration range. Moreover, the osteogenic mechanism of La-based biomaterials remains unknown up to now.

Besides chemical components, the hierarchical porous structures of biomaterials significantly affect their biological performances.[19,20] Inspired by the inherent microstructure of human bones, bone scaffolds with the combination of macropores and mesopores have been developed to enhance new bone regeneration.[21] Three-dimensional (3D) macropores with diameters of >100 μm can act as channels for nutrition transportation, cell migration and bone tissue in-growth.[20,21] Moreover, mesoporous calcium silicate (MCS) nanoparticles possess intrinsic textural characteristics including a large pore volume and a high surface area, which provide great bioactive sites for mediating bone regeneration.[22,23] The nano-topography derived from mesoporous nanoparticles positively modulates cellular responses such as cell proliferation and osteogenic differentiation.[24] Unfortunately, the porous MCS scaffolds are too brittle to employ as bone repair materials. The above disadvantage may be overcome by the combination of MCS nanoparticles with biocompatible CTS. The porous MCS/CTS scaffolds simultaneously possess the advantages of organic–inorganic composites for treating critical-sized bone defects.

In this work, we firstly constructed La-doped mesoporous calcium silicate (La-MCS)/CTS porous scaffolds by a freeze-drying method. The La^{3+} ions can be released from La-MCS/CTS scaffolds in a sustained manner, whose release concentrations were mainly related to the degradation rates of biomaterials. The as-released La^{3+} ions from the scaffolds played an important role in enhancing the proliferation and osteogenic differentiation of BMSCs *via* activating the TGF-β signal pathway. As compared with the MCS/CTS scaffolds without doping La element, the La-MCS/CTS scaffolds significantly accelerate new bone deposition, as confirmed by *in vivo* rat cranial bone defect models.

Experimental

Preparation of MCS and La-MCS nanoparticles

Pure MCS and La-MCS nanoparticles were fabricated by a sol–gel self-assembly (SGSA) method. The as-obtained La-MCS nanoparticles with Ca/La molar ratios of 3 : 1 and 5 : 1 were abbreviated as Ca3La1 and Ca5La1, respectively. For the preparation of pure MCS nanoparticles, 1.76 g of cetyltrimethyl ammonium bromide (CTAB) and 3.20 ml of $NH_3{\cdot}H_2O$ solution were dissolved in 561 ml of deionized water at room temperature for 30 min. 9.33 ml of tetraethyl orthosilicate (TEOS) and 9.73 g of $Ca(NO_3)_2$ were successively added into the above solution, followed by ageing for 20 h. The MCS nanoparticles were obtained after the precipitates were filtered from the solution, washed with ethanol and water mixed solution, and then sintered at a high temperature of 550 °C. The La-MCS nanoparticles including Ca3La1 and Ca5La1 were synthesized by the same method except that part of $Ca(NO_3)_2$ was replaced by $La(NO_3)_3$.

Preparation of La-MCS/CTS scaffolds

0.80 g CTS powders (deacetylation degree of more than 90%, Runjie chemical reagent Co. Ltd, Shanghai, China) and 0.80 g La-MCS nanoparticles were successfully added to an acetic acid solution (20 ml, 2.0 vol%), followed by violent stirring for 2 h. The mixtures were injected into a 24-well plate. The samples were frozen at −20 °C for 12 h, transferred to freeze-drying equipment, and then lyophilized at −60 °C for 72 h. The as-obtained scaffolds were treated with 120 ml sodium hydroxide (10.0 wt%) in order to neutralize the remaining acetic acid in the scaffolds. Finally, La-MCS/CTS scaffolds were washed with deionized water, and freeze-dried again.

Characterization

The phase structures and functional groups of samples were characterized by X-ray powder diffraction (XRD, D/MAX-111 C) and a Fourier transform infrared spectrometer (FTIR, PerkinElmer) was used to investigate the functional groups of the samples in the wavenumber range of 4000 to 400 cm^{-1}. Field-emission scanning electron microscopy (FESEM, JSM-6380LV) with energy-dispersive spectrometry (EDS) was used to characterize the morphologies and elements of samples. La-doped calcium silicate powders were visualized using electron microscopy (TEM; JEOL2100) and the N_2 adsorption–desorption isotherms of samples measuring the specific surface area and pore volume were determined by the Brunauer–Emmett–Teller (BET) method at 77 K. The compressive strengths of Ca3La1/CTS scaffolds and Ca5La1/CTS scaffolds (r = 0.65 cm, h = 1.5 cm) were analysed using a microcomputer controlled electronic universal testing machine (WDW-0.5C, Shanghai Hualong Microelectronics Co. Ltd, China) with a compression speed of 5 mm min^{-1}, and each sample was tested three times with the same method. *In vitro* release tests of Ca3La1/CTS scaffolds were performed by soaking 0.04 g samples in 9 ml deionized water. At different time points, the concentrations of La^{3+} ions were analyzed by inductively coupled plasma/optical emission spectrometry (ICP; iCAP 7000, Thermo Fisher).

Isolation of bone marrow-derived mesenchymal stem cells (BMSCs) and cell culture

Bone marrow-derived mesenchymal stem cells (BMSCs) were isolated from Sprague-Dawley male rats obtained from Silaike (Shanghai, China). The tibia and the femur were isolated, and all bone marrow was flushed out. The whole washouts were collected, sifted with a 400-mesh filter, centrifuged and treated with erythrocyte lysis buffers. rBMSCs were maintained in α-Modified Eagle Medium (α-MEM, Hyclone, USA), supplemented with 10% fetal bovine serum (FBS, Gibco, USA) and 1/100 penicillin–streptomycin (Gibco), and cells at 3–5 passages were used for subsequent experiments. rBMSCs were kept in a humidified atmosphere containing 5% CO_2 at 37 °C.

For osteogenic differentiation, the culture medium was supplemented with 10^{-2} M β-sodium glycerophosphate, 50 μg ml^{-1} L-ascorbic acid and 10^{-7} M dexamethasone. The experimental protocol was approved by the Research Ethics Committee of the Shanghai Sixth People's Hospital-affiliated Shanghai Jiao Tong University and conducted in compliance with regulations of the Helsinki Declaration.

Morphology analysis

Approximately 2×10^5 rBMSCs were seeded on the MCS/CTS, Ca5La1/CTS and Ca3La1/CTS scaffolds (60 mg) and the scaffolds were placed in a 24-well plate. Cell attachment and distribution in scaffolds were evaluated at day 3. Scaffolds were fixed, dehydrated and coated with gold. Then the morphology was observed by scanning electron microscopy (SEM, Hitachi, S-4700, Japan).

Cell counting kit-8 (CCK-8)

A number of 1×10^4 rBMSCs were seeded in a 96-well culture plate, incubated with MCS/CTS, Ca5La1/CTS or Ca3La1/CTS scaffolds (6 mg) and cultured with normal culture medium for 1, 3 and 7 days, respectively. Then the cell viability at these three time points was measured by CCK-8 assay in accordance with the manufacturer's instructions (Beyotime, Nantong, China). The optical density at 450 nm was gauged by using a microplate reader (Bio-Rad, USA).

Western blot analysis

The scaffolds (60 mg) and rBMSCs were co-incubated on a 6-well plate and cultured with osteoinductive medium for 7 days. After that the total protein was extracted with RIPA lysis buffer (Beyotime, Haimen, China). The protein concentrations in the lysates were measured using a BCA Protein Assay Kit (Cell Signalling Technology). Then, 30 mg protein of total protein was separated by sodium dodecyl sulfate poly-acrylamide gel electrophoresis (SDS-PAGE) and transferred onto polyvinylidene fluoride (PVDF) membranes after electrophoresis. The membranes were washed in Tris-buffered saline 0.1% Tween (TBST) and blocked with 5% skimmed milk for 1 h. Each membrane was incubated with the appropriate primary antibody. BMP-2, p-smad1/5 and β-actin antibodies were purchased from Cell Signaling Technology (Shanghai, China). Horseradish peroxidase (HRP)-conjugated polyclonal goat antibodies were used as secondary antibodies. β-Actin was used as the internal reference.

Real-time polymerase chain reaction (RT-PCR)

rBMSCs were incubated with MCS/CTS, Ca5La1/CTS or Ca3La1/CTS scaffolds (6 mg) in osteoinductive culture medium for 7 days. Then, total RNA was extracted using TRIzol (Invitrogen, USA) according to the manufacturer's instructions. Then, RNA was reverse-transcribed and the expression of ALP, OCN and Runx2 at the mRNA level was detected by RT-PCR. The procedure for RT-PCR is as follows: 95 °C for 30 s; 40 cycles at 95 °C for 10 s and at 60 °C for 30 s. The expression of mRNAs was calculated by the 2-ΔΔCt method, and β-actin was used as a reference gene. The primers (BioTNT, Shanghai, China) for RT-PCR are designed as follows: ALP, forward: 5′ CGT TGA CTG TGG TTA CTG CTG 3′ and reverse: 5′ CTT CTT GTC CGT GTC GCT 3′; OCN, forward: 5′ CAG ACA AGT CCC ACA CAG CA 3′ and reverse: 5′ CCA GCA GAG TGA GCA GAG AGA 3′; Runx2, forward: 5′ ATC ATT CAG TGA CAC CAC CAG 3′ and reverse: 5′ GTA GGG GCT AAA GGC AAA AG 3′; and β-actin, forward: 5′ CCT CTA TGC CAA CAC AGT 3′ and reverse: 5′ AGC CAC CAA TCC ACA CAG 3′.

Alizarin red staining

1×10^5 rBMSCs were seeded on a 24-well plate with MCS/CTS, Ca5La1/CTS and Ca3La1/CTS scaffolds (60 mg), incubated with osteogenic induction medium for 14 days. The culture medium was renewed every 48 h. Afterwards, the cells were fixed with 4% paraformaldehyde and stained with alizarin red. Then the cells were visualized under a light microscope (Leica, Germany).

Alkaline phosphatase (ALP) staining

NBT (nitro-blue tetrazolium chloride) and BCIP (5-bromo-4-chloro-30-indolyphosphate *p*-toluidine salt) were used to analyse the alkaline phosphatase activity. rBMSCs were seeded on a 24-well culture plate at 1×10^5 cells per well, cultured with MCS/CTS, Ca5La1/CTS and Ca3La1/CTS scaffolds (60 mg) and incubated with osteogenic induction medium. The culture medium was renewed every 48 h. 7 days post osteogenic differentiation induction, the cells were fixed with 4% paraformaldehyde. Furthermore, the NBT–BCIP substrate was added to the cells and incubated with the cells for approximately 20 minutes. Finally, the cells were observed under a light microscope (Leica, Germany).

Bilateral critical-sized calvarial-defect model

Twenty Sprague-Dawley male rats (body weight: 300–350 g) obtained from Silaike (Shanghai, China) were employed to establish the bilateral critical-sized calvarial-defect model and to evaluate the bone regeneration ability of MCS/CTS, Ca5La1/CTS or Ca3La1/CTS scaffolds. During all the operative process, the animals were anesthetized using chloral hydrate through intraperitoneal injection. A 1.5–2.0 cm sagittal incision was created on the scalp, and two parietal defects were created (diameter: 5 mm, thickness: 2 mm) in the central area using an electric trephine drill (Nouvag AG; Goldach, Switzerland), and MCS/CTS, Ca5La1/CTS or Ca3La1/CTS scaffolds (6 mg, n = 6 per group) were implanted. Then the incisions were closed with 4-0 silk sutures to achieve primary closure. All the animals were permitted access to food and water freely and underwent daily observation for potential complications or abnormal behaviour. All experimental procedures were approved by the Animal Research Committee of the Sixth People's Hospital of Shanghai Jiao Tong University.

Micro-CT scanning

Twelve-weeks after rat animal model establishment, all rats were sacrificed *via* an over-dose of chloral hydrate, and the cal-

varias were obtained. The calvarias were scanned with a micro-CT scanner (Bruker, Germany) and the 2-D images were analyzed using CTAn software (Bruker, Germany). The bone mineral density (BMD) and bone volume per tissue volume (BV/TV) were determined.

Immunofluorescence staining

Polychrome sequential fluorescent labelling was conducted to observe the rate of new bone formation and mineralization at week 12. At 2, 4 and 6 weeks post surgery, the rats were intraperitoneally injected with fluorochromes (25 mg kg^{-1} tetracycline, Sigma, USA; 30 mg kg^{-1} alizarin reds, Sigma; and 20 mg kg^{-1} calcein, Sigma) under anaesthesia. The rats were sacrificed at 12 weeks post surgery, and the defected calvarias were collected. After dehydration in gradient alcohol, the undecalcified specimens were embedded in poly-methylmethacrylate and sectioned to 150 μm thickness in the orientation of the sagittal surface. Then fluorescence signals were observed using a confocal microscope (Leica, Germany).

Histology

The calvarias were pre-treated as aforementioned and sectioned to 150 μm thickness in the orientation of the sagittal surface. Histological analyses were performed by using Van Gieson's picrofuchsin staining according to standard procedures.

Statistical analysis

Data are presented as mean ± standard deviation (SD) and were compared by ANOVA with Tukey's multiple comparison *post hoc* test. All data were analysed using SPSS 19.0 software (SPSS Inc., USA). Two-sided $P < 0.05$ was considered statistically significant.

Results and discussion

Morphology and structure of La-MCS nanoparticles

La^{3+} ions have beneficial and positive effects on bone cells and tissues in the safe concentration range, while the high concentrations lead to toxicity.[15,17] In order to control the La^{3+} concentrations, an alternative strategy is to incorporate the La element into MCS nanoparticles. In this work, the La-MCS nanoparticles were formed by using CTAB as an organic template. The addition of CTAB in deionized water induced the formation of micelles by the self-assembly procedure. The Ca^{2+}, La^{3+} and SiO_3^{2-} ions attached to the micelle surfaces *via* electrostatic forces or hydrogen bonding interactions, and then formed La-MCS precursors under the catalysis of a $NH_3{\cdot}H_2O$ solution. The mesopores were produced after the removal of CTAB *via* high-temperature sintering (Fig. 1).[25] The morphologies of La-MCS nanoparticles were detected in the SEM and TEM images (Fig. 1a and b). These nanoparticles presented irregular shapes, whose diameters were mainly distributed around 20 nm (Fig. 1a). Interestingly, many bright spots were detected within the La-MCS nanoparticles, demonstrating

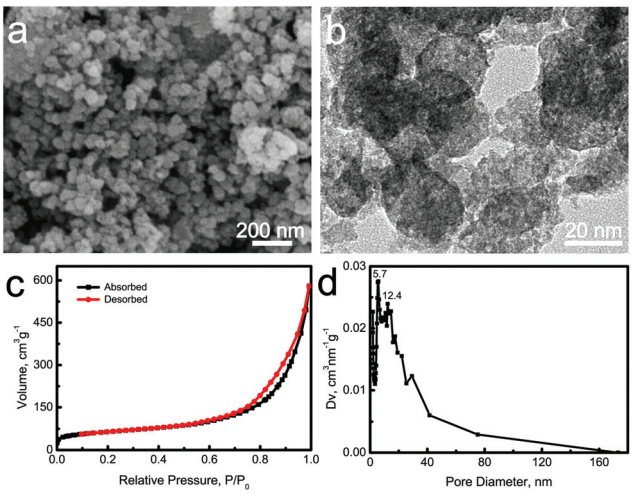

Fig. 1 (a) SEM image; (b) TEM image; (c) nitrogen adsorption–desorption isotherms and (d) BJH pore size distribution curve of La-MCS nanoparticles.

the presence of the mesoporous structure (Fig. 1b). The type IV isotherms and type H3 hysteresis loops in Fig. 1c revealed that the mesopores exhibited irregular shapes. According to the BJH model, the mesopore sizes of La-MCS nanoparticles were mainly distributed at approximately 5.7 and 12.4 nm (Fig. 1d). The BET surface areas of La-MCS nanoparticles were increased up to 222.1 $m^2\ g^{-1}$. Notably, the La^{3+} ions played a significant role in regulating the morphology of La-MCS nanoparticles. In the absence of La^{3+} ions, the pure $CaSiO_3$ particles showed a spherical shape with diameters of approximately 200 nm (Fig. S1†). The particle sizes of the La-MCS nanoparticles were much smaller than those of the $CaSiO_3$ particles (Fig. 1 and S1†). The reason was attributed to the possibility that the greater electrostatic binding force between La^{3+} and SiO_3^{2-} ions than that between Ca^{3+} and SiO_3^{2-} ions remarkably decreased the sizes of La-MCS precursors.

The phase structure of the La-MCS nanoparticles was characterized using the XRD pattern. The broad peak at 2θ = 20–30° revealed that these nanoparticles presented an amorphous characteristic (Fig. 2a). Moreover, the FTIR spectrum showed the functional groups of the La-MCS nanoparticles (Fig. 2b). The band at 1629 cm^{-1} corresponded to the O–H bending vibration of adsorbed water on the nanoparticle sur-

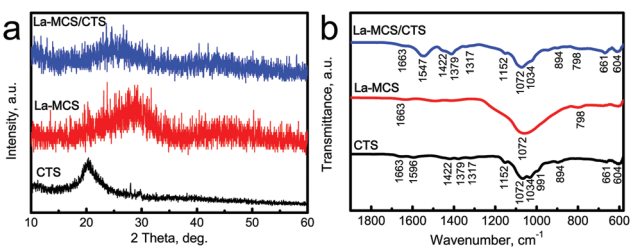

Fig. 2 (a) XRD patterns and (b) FTIR spectra of CTS powders, La-MCS nanoparticles and La-MCS/CTS scaffolds.

faces. The characteristic bands due to the Si–O–Si stretching vibration located at 800 and 1072 cm^{-1}.[26]

Morphology and structure of La-MCS/CTS scaffolds

La-MCS/CTS scaffolds were fabricated by a lyophilization method. During the freeze-drying procedure, the CTS and La-MCS mixed solutions were converted to La-MCS/CTS porous scaffolds by using ice crystals as templates. The volatilization of ice crystals contributed to forming three-dimensional (3D) macropores with a size of ~200 μm within the La-MCS/CTS scaffolds (Fig. 3a). The high-resolution SEM images revealed that lots of La-MCS nanoparticles were uniformly distributed on the macropore walls (Fig. 3b). The chemical components of the La-MCS/CTS scaffolds were determined using elemental distribution images and the EDS spectrum (Fig. 3c–f). The Si, Ca and La elements were derived from the La-MCS nanoparticles, and the C element was derived from the CTS.

The structures of the La-MCS/CTS scaffolds were characterized using XRD patterns and FTIR spectra, and pure CTS powders and La-MCS nanoparticles as control groups (Fig. 2). Since both the CTS and La-MCS were non-crystalline materials, only a broad peak due to the amorphous structure was observed at around 2θ = 25° for the La-MCS/CTS scaffolds (Fig. 2a). The functional groups of the composite scaffolds mainly originated from the La-MCS and CTS (Fig. 2b). The N–H deformation and N–H wagging vibration bands of the amino group located at 1596 and 894 cm^{-1}, respectively.[27,28]

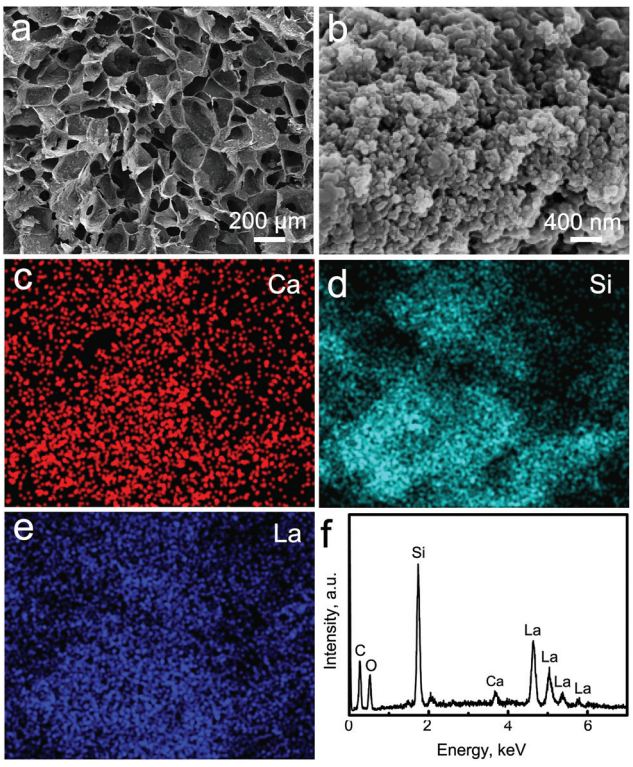

Fig. 3 Characterization of La-MCS/CTS scaffolds: (a, b) SEM images; (c, d, e) element distribution images; and (f) EDS spectrum.

The characterized band due to C–N in the secondary amide groups located at 1317 cm^{-1}, while that due to C–N in the primary amide groups located at 1422 and 1379 cm^{-1}.[28] The bands at 1152 and 1072 cm^{-1} were ascribed to the bridge oxygen stretching vibration and C–O stretching vibration, respectively.[28] The characteristic bands due to La-MCS and CTS were observed in the FTIR spectrum of La-MCS/CTS scaffolds (Fig. 2b).

Mechanical properties and *in vitro* degradability of La-MCS/CTS scaffolds

The compression strengths of Ca3La1/CTS scaffolds and Ca5La1/CTS scaffolds were tested under the same conditions, as shown in Fig. 4. With increasing external force, the macropores of these scaffolds were damaged. The corresponding compression strengths reached respectively at 0.19 MPa and 0.15 MPa, which were matched with trabecular bone (0.1–0.5 MPa).[29] In addition, both the scaffolds were ductile materials, so they became tight with further increasing pressure after the macropores were destroyed completely.

The *in vitro* degradation performance of Ca3La1/CTS scaffolds was determined by soaking them in deionized water at 37 °C. The degradation rate (η) of the scaffolds was calculated according to the formula: $\eta = (W - W_0)/W$, where W is the original weight of scaffolds and W_0 is the weight of scaffolds after 7 days. The degradation rate of Ca3La1/CTS and Ca5La1/CTS scaffolds arrived at 13.41% and 17.27%, respectively. During the degradation process, the Ca, Si and La ions were gradually released from the scaffolds into the release media (Fig. S2†). In the initial stage of day 1, all ions had a great release rate because of the concentration gradient between the scaffolds and release media. When the degradation of the scaffolds arrived at dynamic equilibrium, the release rate began to decrease. The *in vitro* degradation of Ca3La1/CTS scaffolds has great effects on the surface morphologies, although the macropores did not change remarkably between before and after degradation (Fig. 3 and S3†). The La-MCS nanoparticles were uniformly dispersed on the macropore walls (Fig. 3b). After *in vitro* degradation for 7 days, the smaller nanoparticles gradually disappeared, and many larger particles with irregular shapes were produced (Fig. S3b†). The above changes were attributed to the dissolution–recrystallization process of the La-MCS nanoparticles within the scaffolds.

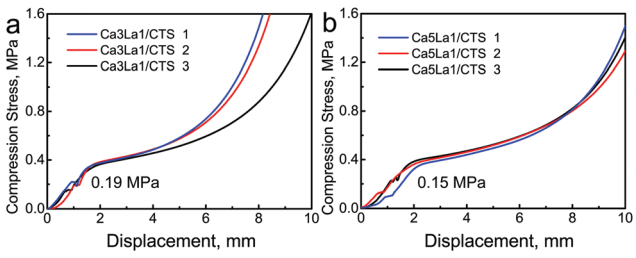

Fig. 4 The mechanical properties of La-MCS/CTS scaffolds: (a) Ca3La1/CTS scaffolds; (b) Ca5La1/CTS scaffolds.

Based on the Ostwald ripening model,[30,31] the smaller particles in the scaffolds easily dissolved into the release media, while the bigger particles tended to grow further (Fig. S3b†).

Ca3La1/CTS scaffolds promote rBMSC proliferation *in vitro*

The biological properties of these three scaffolds were evaluated. rBMSCs were co-cultured with MCS/CTS, Ca5La1/CTS or Ca3La1/CTS scaffolds, and SEM showed that rBMSCs adhered and distributed to the surface of scaffolds, and the cell number on the surface of Ca5La1/CTS or Ca3La1/CTS scaffolds seemed to outnumber the MCS/CTS scaffold (Fig. 5a–c). To validate this phenomenon, the cell viability of co-cultured rBMSCs was determined, and the results showed that either Ca5La1/CTS or Ca3La1/CTS scaffolds significantly promoted cell proliferation at all tested time points (Fig. 5d).

As is well known, the structure, chemical composition and phase were significant influencing factors on the biocompatibility of scaffolds.[32] The La-MCS/CTS scaffolds harboured the mesoporous structure, the pore size of which was approximately 200 μm, which permitted the rapid adhesion and spreading of rBSMCs.[33–35] In previous work, it was found that both CS and CTS possessed prominent biocompatibility and latent capacity for biomedical applications.[36–38] Interestingly, both the structure and chemical composition of the La-MSC/CTS scaffolds provided a basis for rapid cell adhesion and proliferation. Furthermore, a peak of cell adhesion and proliferation occurred in the Ca3La1/CTS group. Previous studies reported that the suitable concentration of Ca^{2+} and La^{3+} ions facilitated the proliferation of rBMSCs.[39,40] The better biocompatibility possessed by the Ca3La1/CTS scaffolds is attributed not only to the mesoporous structure which provided the foundation for cell adhesion and proliferation, but also to a more appropriate ionic environment.

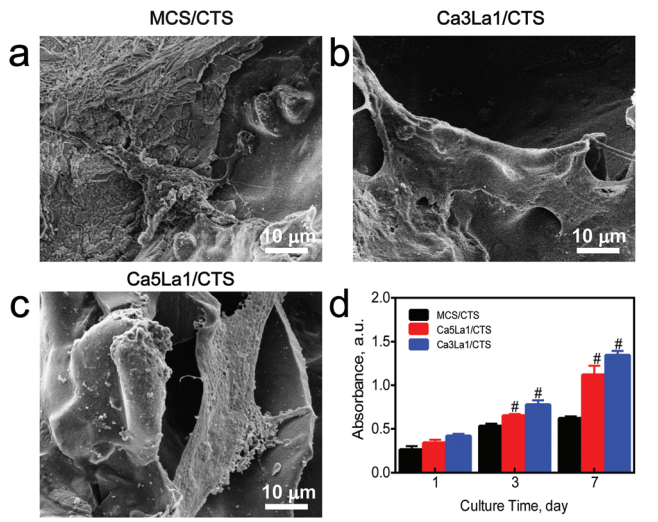

Fig. 5 Ca3La1/CTS scaffolds promoted BMSC proliferation: (a) the distribution of BMSCs on the surface of MCS/CTS, Ca5La1/CTS or Ca3La1/CTS scaffolds; (b) cell viability of BMSCs co-cultured with MCS/CTS, Ca5La1/CTS and Ca3La1/CTS scaffolds. #$p < 0.05$, all experiments were performed in triplicate.

Ca3La1/CTS scaffolds facilitate the expression of osteogenic markers in rBMSCs *in vitro*

The ability of MCS/CTS, Ca5La1/CTS and Ca3La1/CTS scaffolds in promoting rBMSC osteogenesis was measured. As expected, Ca3La1/CTS scaffolds significantly promoted the expression of osteogenic markers, such as ALP, OCN and Runx2 (Fig. 6a–c).[41–43] The TGF-β signal pathway is known to be a critical pathway in the osteogenic differentiation of BMSCs.[44] BMP-2, which was identified as one of the TGF family members, combined to the Type II receptor and recruited Type I.[45] With the phosphorylation of the Type II receptor, Type I was activated. The Type I receptor, in turn, prompted the phosphorylation of receptor-activated Smads (Smad1/5).[46] Once phosphorylated, the heteromeric complex p-Smad 1/5 combined with the co-mediator Smad (Smad4) and then translocated into the nucleus, which finally activated osteogenic-related genes.[47] The western blot analysis was used to probe the underlying mechanism of the ossification of MCS/CTS, Ca5La1/CTS or Ca3La1/CTS scaffolds. The results showed that the level of BMP-2 was obviously increased by co-incubation of the Ca5La1/CTS and Ca3La1/CTS scaffolds (Fig. 6d), which paralleled the upregulation of p-Smad1/5 (Fig. 6d).

Alizarin red staining was performed to visualize the calcium deposition in the extracellular matrix, which was

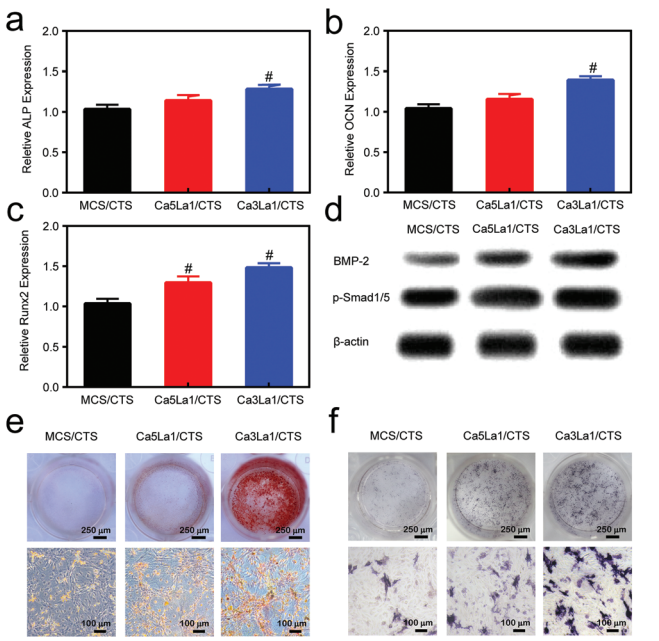

Fig. 6 Osteogenic markers were augmented by Ca3La1/CTS scaffolds. The expression of (a) ALP, (b) OCN and (c) Runx2 at the mRNA level which was evaluated after 7 days' co-incubation; (d) the stable cell lines were subjected to western blotting and detected for BMP-2, p-Smad1/5, normalized to β-actin. (e) Alizarin red staining; (f) ALP staining. #$p < 0.05$, all experiments were performed in triplicate.

considered as the early marker of osteogenesis.[48] Compared with MCS/CTS, Ca3La1/CTS scaffolds significantly promoted osteogenic differentiation as indicated by alizarin red staining (Fig. 6e). BCIP/NBT staining was conducted to analyse the alkaline phosphatase activity. The formation of an insoluble NBT diformazan product which was stained blue indicated the alkaline phosphatase.[49] Fig. 6f indicates that the ALP activity was augmented by the Ca3La1/CTS scaffolds most.

Due to the La^{3+} ions, the TGF-β pathway was activated and the expression of ALP, OCN and Runx2 gene was upregulated,[50] which explained the phenomenon that the La-MCS/CTS scaffolds promoted the osteogenesis of extracorporal rBMSCs. Moreover, the concentration of Ca^{2+} was also the vital point. The osteogenic differentiation can be promoted by the increase in the density of Ca^{2+}.[51] However, the increasing level of Ca^{2+} ions in any form or for any reason finally caused apoptosis.[52] Therefore, an exorbitant concentration of Ca^{2+} showed weaker capability in promoting the osteogenic differentiation than the appropriate concentration.

Ca3La1/CTS scaffolds promote bone formation *in vivo*

The Ca3La1/CTS scaffold application in bone formation was tested in a bilateral critical-sized calvarial-defect rat model. Compared with MCS/CTS, bone defects treated with Ca5La1/CTS or Ca3La1/CTS scaffolds showed signs of bone formation as indicated by CT scanning (Fig. 7a). Furthermore, BMD and BV/TV in Ca5La1/CTS or Ca3La1/CTS scaffold-treated rats were significantly higher than those in rats treated with MCS/CTS (Fig. 7b and c).[53,54] Notably, these parameters in Ca3La1/CTS treated rats reached the peak among the groups. Additionally, bone formation and mineralization were also measured. The fluorescence signaling of tetracycline, alizarin red and calcein indicated the loci of new bone formation (Fig. 8a).[55–57] The fluorescence density in Ca5La1/CTS and Ca3La1/CTS scaffold-treated rats was significantly higher than that in the MCS/CTS group (Fig. 8b).

Van Gieson's picrofuchsin staining was used to determine the osteogenic induction ability of scaffolds.[58,59] As shown in Fig. 9, Ca5La1/CTS and Ca3La1/CTS scaffolds significantly promoted osteogenesis compared with MCS/CTS. The most obviously stained ossein occurred in the Ca3La1/CTS scaffold group, which indicated that Ca3La1/CTS scaffolds harboured more prominent ability in promoting bone formation than the Ca5La1/CTS scaffolds.

In keeping with the *in vitro* experiment, intracorporal new bone formation was also promoted by the La-MCS/CTS scaffolds. Because of the enhanced osteogenesis of rBMSCs which indirectly regulated the bone resorption function of osteoclasts,[60] which finally accelerated the bone regeneration, the excellent osteoinductivity of La-MCS/CTS scaffolds was verified *in vivo*. Ossein, a great part of the bone organic matrix, provided the framework for calcium deposition, which played an important role in maintaining the integrity of the bone structure and bone biomechanical properties.[61,62] Equally, the more stained ossein was exhibited as a consequence of the enhanced osteogenic differentiation affected by the La-MCS/CTS scaffolds. To sum up, the results mentioned above

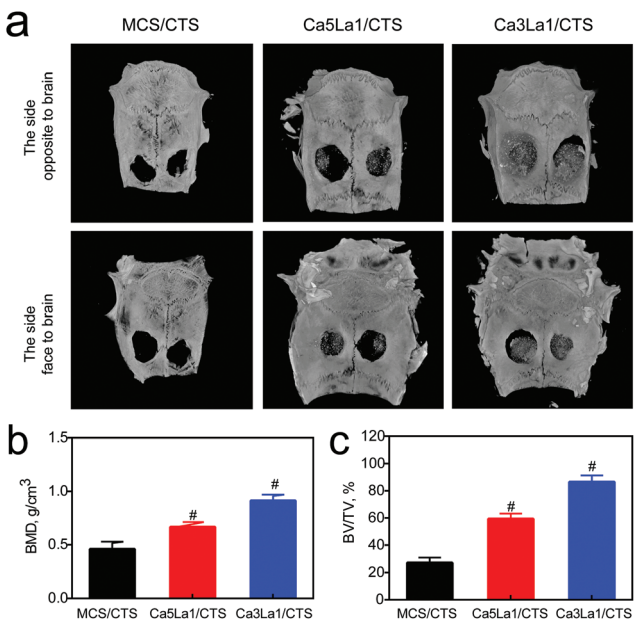

Fig. 7 Ca3La1/CTS scaffolds promoted bone formation. (a) Representative images for micro-CT scanning; (b) BMD; (c) BV/TV. #p < 0.05 *versus* MCS/CTS, n = 6 per group.

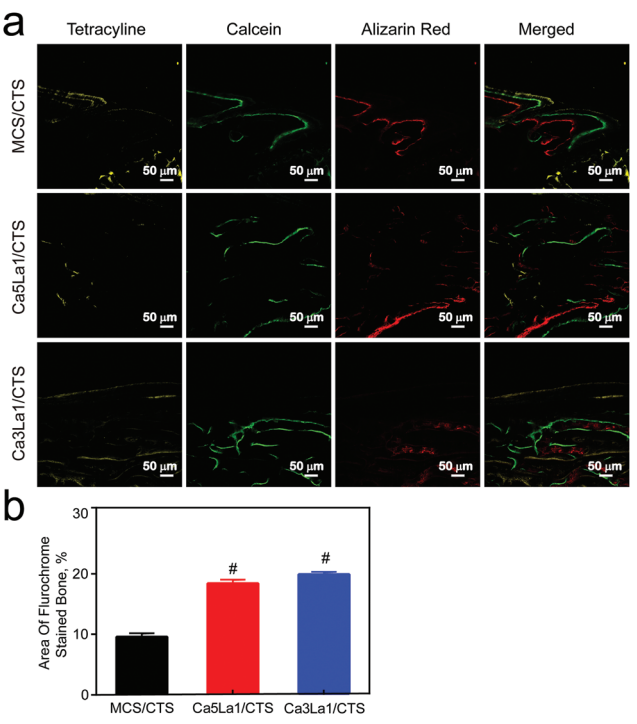

Fig. 8 Fluorescence density was high in Ca3La1/CTS scaffold-treated rats. (a) Representative image of fluorescence assay for tetracycline, alizarin red and calcein; (b) statistical evaluation of the fluorochrome area. #p < 0.05 *versus* MCS/CTS, n = 6 per group.

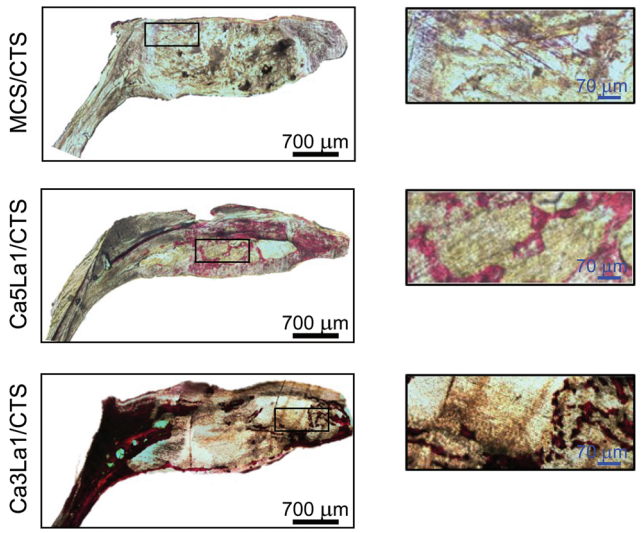

Fig. 9 Representative image of Van Gieson's picrofuchsin staining. The red stained area was ossein.

reached a point where the Ca3La1/CTS scaffolds effectively induce osteogenesis *in vivo*.

Conclusions

In the present study, we firstly constructed three-dimensional La-MCS/CTS porous scaffolds by a freeze-drying method. The Ca3La1/CTS scaffolds could support the adhesion, spreading and proliferation of rBMSCs, and harbor the ability in promoting bone regeneration. OCN, Runx2 and ALP are well characterized biomarkers for osteogenesis and their expression is associated with osteogenesis. As expected, the Ca3La1/CTS scaffolds significantly upregulated the expression of these indicators, indicating that MCSC scaffolds could facilitate bone formation. Furthermore, the underlying mechanism of the ossification of the Ca3La1/CTS scaffolds was also explored. The result of western blotting indicated that activating the TGF-β pathway was the vital link. Additionally, post Ca3La1/CTS scaffold injection, BV/TV and BMD were increased which suggested new bone formation *in vivo*. As the La-MCS/CTS scaffolds possessed favourable mechanical properties and degradation, the Ca3La1/CTS scaffolds performed well as a bone void filler. Moreover, micro-CT, Van Gieson's picrofuchsin staining and fluorescence assay further validated this phenomenon. These findings support the notion that Ca3La1/CTS scaffolds could promote the osteogenic differentiation of BMSCs, which could possibly be applied in clinics for patients with bone defects.

Conflicts of interest

There are no conflicts to declare.

Acknowledgements

This research was supported by the Natural Science Foundation of China (no. 51372152) and the Innovation Foundation of Shanghai Education Committee (no. 14ZZ124).

Notes and references

1 H. W. Kang, S. J. Lee, I. K. Ko, C. Kengla, J. J. Yoo and A. Atala, *Nat. Biotechnol.*, 2016, **34**, 312–319.
2 A. Zheng, L. Y. Cao, Y. Liu, J. Wu, D. Zeng, L. Hu, X. Zhang and X. Jiang, *Carbohydr. Polym.*, 2018, **199**, 244–255.
3 M. Liu, X. Zeng, C. Ma, H. Yi, Z. Ali, X. Mou, S. Li, Y. Deng and N. He, *Bone Res.*, 2017, **5**, 75–94.
4 D. Tang, R. S. Tare, L. Y. Yang, D. F. Williams, K. L. Ou and R. O. Oreffo, *Biomaterials*, 2016, **83**, 363–382.
5 B. J. Klotz, D. Gawlitta, A. J. Rosenberg, J. Malda and F. P. Melchels, *Trends Biotechnol.*, 2016, **34**, 394–407.
6 H. Xu, Y. W. Ge, J. W. Lu, Q. F. Ke, Z. Q. Liu, Z. A. Zhu and Y. P. Guo, *Chem. Eng. J.*, 2018, **354**, 285–294.
7 Q. Q. Yao, J. G. L. Cosme, T. Xu, J. M. Miszuk, P. H. S. Picciani, H. Fong and H. L. Sun, *Biomaterials*, 2017, **115**, 115–127.
8 R. Shahsavari and S. H. Hwang, *Langmuir*, 2018, **34**, 12154–12166.
9 A. Oryan and S. Alidadi, *Life Sci.*, 2018, **201**, 45–53.
10 J. Zhang, H. J. Zhou, K. Yang, Y. Yuan and C. S. Liu, *Biomaterials*, 2013, **34**, 9381–9392.
11 M. Sepantafar, H. Mohammadi, R. Maheronnaghsh, L. Tayebi and H. Baharvand, *Ceram. Int.*, 2018, **44**, 11003–11012.
12 J. Costa-Rodrigues, S. Reis, A. Castro and M. H. Fernandes, *Stem Cells Int.*, 2016, 5653275.
13 E. B. Hunziker, L. Enggist, A. Kuffer, D. Buser and Y. Liu, *Bone*, 2012, **51**, 98–106.
14 C. J. Deng, Q. Yang, X. L. Sun, L. Chen, C. Feng, J. Chang and C. T. Wu, *Appl. Mater. Today*, 2018, **10**, 203–216.
15 J. Bai, X. H. Wang, C. J. Zhang, J. Huang and W. E. G. Muller, *Biometals*, 2018, **31**, 771–784.
16 J. F. Cawthray, D. M. Weekes, O. Sivak, A. L. Creagh, F. Ibrahim, M. Iafrate, C. A. Haynes, K. M. Wasan and C. Orvig, *Chem. Sci.*, 2015, **6**, 6439–6447.
17 T. Fumoto, M. Ito and K. Ikeda, *J. Bone Miner. Metab.*, 2014, **32**, 484–493.
18 G. Pagano, M. Guida, F. Tommasi and R. Oral, *Ecotoxicol. Environ. Saf.*, 2015, **115**, 40–48.
19 Y. X. Chen, J. Q. Yu, Q. F. Ke, Y. S. Gao, C. Q. Zhang and Y. P. Guo, *Chem. Eng. J.*, 2018, **341**, 112–125.
20 F. Yang, J. W. Lu, Q. F. Ke, X. Y. Peng, Y. P. Guo and X. T. Xie, *Sci. Rep.*, 2018, **8**, 7345.
21 W. Tang, D. Lin, Y. M. Yu, H. Y. Niu, H. Guo, Y. Yuan and C. S. Liu, *Acta Biomater.*, 2016, **32**, 309–323.
22 X. Qi, P. Pei, M. Zhu, X. Y. Du, C. Xin, S. C. Zhao, X. L. Li and Y. F. Zhu, *Sci. Rep.*, 2017, **7**, 42556.

23 F. F. Wang, D. Zhai, C. T. Wu and J. Chang, *Nano Res.*, 2016, **9**, 1193–1208.
24 Q. L. Huang, T. A. Elkhooly, X. J. Liu, R. R. Zhang, X. Yang, Z. J. Shen and Q. L. Feng, *Colloids Surf., B*, 2016, **145**, 37–45.
25 J. Zhu, R. Z. Liang, C. Sun, L. Z. Xie, J. Wang, D. Y. Leng, D. M. Wu and W. H. Liu, *PLoS One*, 2017, **12**(8), e0182583.
26 W. C. Xue, A. Bandyopadhyay and S. Bose, *Acta Biomater.*, 2009, **5**, 1686–1696.
27 T. M. Tamer, M. A. Hassan, A. M. Omer, K. Valachova, M. S. M. Eldin, M. N. Collins and L. Soltes, *Carbohydr. Polym.*, 2017, **169**, 441–450.
28 G. F. Jiang, J. P. Weng, L. P. Kong, H. Xu and M. Z. Liu, *Mater. Lett.*, 2017, **189**, 122–125.
29 A. J. W. Johnson and B. A. Herschler, *Acta Biomater.*, 2011, **7**, 16–30.
30 B. Zhao, G. Shao, B. B. Fan, W. Y. Zhao, Y. J. Xie and R. Zhang, *J. Mater. Chem. A*, 2015, **3**, 10345–10352.
31 A. Fadli, A. Amri, E. O. Sari, Iwantono and A. Adnan, *Int. J. Technol.*, 2017, **8**, 1445–1454.
32 Y. X. Chen, R. Zhu, Q. F. Ke, Y. S. Gao, C. Q. Zhang and Y. P. Guo, *Nanoscale*, 2017, **9**, 6765.
33 W. Cui, Q. Q. Liu, L. Yang, K. Wane, T. F. Sun, Y. H. Ji, L. P. Liu, W. Yu, Y. Z. Qu, J. W. Wang, Z. G. Zhao, J. T. Zhu and X. D. Guo, *ACS Biomater. Sci. Eng.*, 2018, **4**, 211–221.
34 M. Castilho, C. Moseke, A. Ewald, U. Gbureck, J. Groll, I. Pires, J. Tessmar and E. Vorndran, *Biofabrication*, 2014, **6**(1), 015006.
35 R. R. Zhang, T. A. Elkhooly, Q. L. Huang, X. J. Liu, X. Yang, H. Yan, Z. Y. Xiong, J. Ma, Q. L. Feng and Z. J. Shen, *J. Biomed. Mater. Res., Part A*, 2018, **106**, 1896–1902.
36 X. Wang, L. Wang, Q. Wu, F. Bao, H. Yang, X. Qiu and J. Chang, *ACS Appl. Mater. Interfaces*, 2018, DOI: 10.1021/acsami.8b17754, ISSN: 1944-8252, PubMed ID: 30543278.
37 E. Athanasiadou, M. Paschalidou, A. Theocharidou, N. Kontoudakis, K. Arapostathis and A. Bakopoulou, *Dent. Mater.*, 2018, **34**, 1797–1813.
38 C. Y. Goh, S. S. Lim, K. Y. Tshai, A. El Azab and H. S. Loh, *J. Mater. Sci.*, 2019, **54**, 3403–3420.
39 J. S. Guo, C. Q. Ning and X. Y. Liu, *Colloids Surf., B*, 2018, **164**, 388–395.
40 B. Kruppke, C. Heinemann, A.-S. Wagner, J. Farack, S. Wenisch, H.-P. Wiesmann and T. Hanke, *Dev., Growth Differ.*, 2018, DOI: 10.1111/dgd.12588, ISSN: 1440-169X, PubMed ID: 30585307.
41 Y. L. Zhang, J. H. Yin, H. Ding, C. Q. Zhang and Y. S. Gao, *Int. J. Biol. Sci.*, 2016, **12**, 776–785.
42 N. Han, Z. C. Li, Z. D. Cai, Z. Q. Yan, Y. Q. Hua and C. Xu, *J. Cell. Mol. Med.*, 2016, **20**, 2173–2182.
43 S. M. Kim, S. W. Yi, H. J. Kim, J. S. Park, J. H. Kim and K. H. Park, *J. Biomed. Nanotechnol.*, 2019, **15**, 113–126.
44 G. Q. Chen, C. X. Deng and Y. P. Li, *Int. J. Biol. Sci.*, 2012, **8**, 272–288.
45 K. Masuhara, T. Nakase, S. Suzuki, K. Takaoka, M. Matsui and H. C. Anderson, *Bone*, 1995, **16**, 91–96.
46 K. Higashi, E. Matsuzaki, Y. Hashimoto, F. Takahashi-Yanaga, A. Takano, H. Anan, M. Hirata and F. Nishimura, *Bone*, 2016, **93**, 1–11.
47 Keriaqie, H. T. Yin and X. U. Yong, *Med. Recapitulate*, 2009, (11), 89–92.
48 A. L. Strong, J. F. Ohlstein, Q. Jiang, Q. Zhang, S. L. Zheng, S. M. Boue, S. Elliott, J. M. Gimble, M. E. Burow, G. D. Wang and B. A. Bunnell, *Stem Cell Res. Ther.*, 2014, **5**, 105.
49 R. Mishra and A. Kumar, *J. Mater. Sci.: Mater. Med.*, 2014, **25**, 1327–1337.
50 B. Arumugam, K. Balagangadharan and N. Selvamurugan, *J. Cell Commun. Signal.*, 2018, **12**, 561–573.
51 D. J. Mason, *Eur. Cells Mater.*, 2004, **7**, 12–25; discussion 25-16.
52 F. McDonald, *Surgeon*, 2004, **2**, 63–69.
53 N. Napoli, M. Chandran, D. D. Pierroz, B. Abrahamsen, A. V. Schwartz, S. L. Ferrari and I. O. F. B. D. W. Grp, *Nat. Rev. Endocrinol.*, 2017, **13**, 208–219.
54 M. Priemel, C. von Domarus, T. O. Klatte, S. Kessler, J. Schlie, S. Meier, N. Proksch, F. Pastor, C. Netter, T. Streichert, K. Puschel and M. Amling, *J. Bone Miner. Res.*, 2010, **25**, 305–312.
55 H. Y. Li, L. Zhao, Y. Xu, T. Y. Zhou, H. C. Liu, N. Huang, J. Ding, Y. Li and L. Ding, *Talanta*, 2018, **185**, 542–549.
56 W. L. Smith, C. A. Buck, G. S. Ornay, M. P. Davis, R. P. Martin, S. Z. Gibson and M. G. Girard, *Copeia*, 2018, **106**, 427–435.
57 C. X. Zhao, Y. Jiao, Z. Gao, Y. L. Yang and H. Li, *J. Photochem. Photobiol., A*, 2018, **367**, 137–144.
58 M. Pangalos, W. Bintig, B. Schlingmann, F. Feyerabend, F. Witte, D. Begandt, A. Heisterkamp and A. Ngezahayo, *J. Bioenerg. Biomembr.*, 2011, **43**, 311–322.
59 X. M. Guan, M. P. Xiong, F. Y. Zeng, B. Xu, L. D. Yang, H. Guo, J. L. Niu, J. Zhang, C. X. Chen, J. Pei, H. Huang and G. Y. Yuan, *ACS Appl. Mater. Interfaces*, 2014, **6**, 21525–21533.
60 H. P. Liu, Z. F. Zhuang, L. L. Zhao, J. L. Qu and X. Y. Deng, *Chin. Opt. Lett.*, 2008, **6**, 882–885.
61 H. Oxlund, L. Mosekilde and G. Ortoft, *Bone*, 1996, **19**, 479–484.
62 A. J. Bailey, S. F. Wotton, T. J. Sims and P. W. Thompson, *Connect. Tissue Res.*, 1993, **29**, 119–132.